

# Progress in Aerodynamic Shape Optimization Based on the Reynolds-Averaged Navier-Stokes Equations

David Koo\*, and David W. Zingg†

*Institute for Aerospace Studies, University of Toronto  
4925 Dufferin St., Toronto, Ontario, M3H 5T6, Canada*

This paper presents the application of an aerodynamic shape optimization methodology, Jetstream, to several cases in order to characterize the methodology and demonstrate its ability to solve challenging problems. In Jetstream, geometry parameterization and mesh movement are integrated by fitting the multi-block structured grids with B-spline volumes and applying mesh movement based on linear elasticity to the control points. Geometry control is achieved through either of two different approaches: using the B-spline surface control points as design variables, or embedding them into within a free-form deformation volume. Spatial discretization of the Reynolds-averaged Navier-Stokes equations is performed using summation-by-parts operators with simultaneous approximation terms at boundaries and block interfaces. The discrete equations are solved iteratively using a parallel Newton-Krylov-Schur algorithm. The discrete-adjoint method is used to calculate the gradients, which are supplied to a sequential quadratic programming optimization algorithm. The first drag minimization problem revisits the single-point lift-constrained drag minimization of the NASA Common Research Model (CRM) wing. Multimodality is studied on the CRM wing, beginning the same problem with a variety of different starting geometries. Results are also presented for the single-point CRM optimization with a 75% and a 100% minimum thickness constraint. The CRM wing-body-tail configuration is then optimized with a trim constraint and including the rotation of the horizontal stabilizer as a design variable. The second problem is a multipoint optimization of the RAE 2822 airfoil in transonic flow. The final two problems test the geometric flexibility and robustness of the aerodynamic optimization method. The first is a planform optimization of a rectangular NACA00012 wing in transonic, viscous flow. The second is a wing tip optimization of a planform based on the Boeing 737-900 wing. Overall, the results demonstrate that the algorithms adopted in Jetstream provide a reliable and effective aerodynamic shape optimization methodology capable of addressing challenging problems involving substantial geometric changes.

## I. Introduction

WITH rising fuel prices and the impending danger of climate change, fuel efficiency has become a top priority in designing the next generation of aircraft. Improved aerodynamics will play a key role in this effort, along with advances in engine technology, biofuels, and materials. The AIAA Aerodynamic Design Optimization Discussion Group (ADODG)<sup>a</sup> was created to bring together researchers from industry and academia to compare different techniques of aerodynamic shape optimization. The group has defined a series of benchmark optimization problems, with varying flow conditions and degrees of freedom. Examples of various aerodynamic shape optimization methodologies and their application to the ADODG test problems can be found in Refs. 1–8. In this paper, our optimization framework Jetstream is used to revisit some of the benchmark cases from the previous ADODG meeting,<sup>9</sup> and to solve some additional interesting design problems to test its robustness and flexibility. The CRM wing is studied in greater detail, and later optimized along with the fuselage, tail and trim constraints. The second case is an RAE 2822 airfoil optimization for

---

\*MAsc

†Professor and Director, J. Armand Bombardier Foundation Chair in Aerospace Flight, Associate Fellow AIAA.

<sup>a</sup><https://info.aiaa.org/tac/ASG/APATC/AeroDesignOpt-DG/default.aspx>

a multi-point objective, as opposed to the single-point optimization which was prescribed as the original benchmark problem. The final two cases involve a greater degree of geometric change, including a planform optimization on a rectangular wing and a nonplanar wingtip optimization. The objective of this study is to characterize the algorithms underlying Jetstream in order to provide an understanding of the properties of the overall methodology. In the remainder of this paper, Section II summarizes the algorithms employed in Jetstream, followed by Section III which presents the results obtained for the optimization problems presented. Examples of recent optimization studies of unconventional aircraft configurations using Jetstream can be found in Gagnon and Zingg<sup>10-12</sup> and Reist and Zingg.<sup>13</sup>

## II. Methodology

### A. Integrated Geometry Parameterization, Control, and Mesh Movement

Jetstream uses a cubic B-spline surface parameterization to accurately fit an aerodynamic surface while providing geometric flexibility.<sup>14</sup> Each block in the multi-block mesh is fitted with a cubic B-spline volume and the control points defining the wing or aircraft surface are manipulated by the optimizer. The procedure for fitting and determining the knot vectors can be found in Lee et al.<sup>9</sup> and Hicken and Zingg.<sup>14</sup>

The control points on the aerodynamic surface can be manipulated directly as the design variables, or they can be changed indirectly using free-form deformation (FFD) geometry control. Conceptually, FFD can be visualized as enclosing the geometry in a larger volume of flexible material and indirectly deforming the geometry by deforming the outer volume. In Jetstream, the embedded objects are taken as the B-spline surface control points defining the geometry, and the FFD volume is a cubic B-spline volume.<sup>10</sup> This maintains an analytical definition of the geometry and allows the mesh movement, to be performed in the same way as with B-spline surface control. Gagnon and Zingg<sup>10</sup> describe the deformation process as a two-level approach: the first level involves the control points defining the FFD volume, the second level involves the control points defining the geometry.

Once the geometry has been modified, the computational mesh is deformed using a linear-elasticity model<sup>15</sup> to propagate displacements from the wing surface to the rest of the mesh. In Jetstream, this mesh movement model is applied to the B-spline control mesh rather than the computational mesh, reducing computational cost while maintaining the original mesh quality.<sup>14</sup> The mesh movement system is defined by:

$$\mathcal{M} = \mathbf{K}(\mathbf{b} - \mathbf{b}^{(0)}) - \mathbf{f} = 0, \quad (1)$$

where  $\mathcal{M}$  are the mesh residuals,  $\mathbf{K}$  is the stiffness matrix,  $\mathbf{b}$  and  $\mathbf{b}^{(0)}$  are the updated and initial control point coordinate column vectors, respectively, and  $\mathbf{f}$  is the force vector implicitly determined from the displaced surface control points. For large shape changes, the mesh movement is performed in a number of increments to reduce cell distortion. Once the control mesh has been deformed, algebraic recomputation of the grid nodes is very quick to perform.

### B. Flow Solver

Jetstream uses a three-dimensional multi-block structured finite-difference solver. A parallel Newton-Krylov-Schur method is used to solve the Reynolds-averaged Navier-Stokes (RANS) equations<sup>16,17</sup> with the Spalart-Allmaras one-equation turbulence model. Spatial discretization of the governing equations is performed using second-order summation-by-parts operators. Boundary and block interface conditions are enforced weakly through simultaneous approximation terms, which allow  $C^1$  discontinuities in the mesh at block interfaces.

The solver begins with an approximate-Newton phase, which uses implicit time-stepping to globalize the solution. Once the flow residual has been reduced by several orders of magnitude, this working solution is used as the initial iterate in an inexact-Newton phase which leads to deep convergence of the residual. The flexible generalized minimal residual (GMRES) method with approximate-Schur parallel preconditioner is used as the linear solver. A scalar artificial dissipation scheme<sup>18,19</sup> is used for the cases in this paper, but matrix dissipation<sup>20</sup> can also be used.

### C. Gradient Evaluation and Optimization Algorithm

The gradients of the aerodynamic functionals are computed using the discrete-adjoint method, which is applied by formulating the problem as:

$$\min \mathcal{J}(\mathbf{v}, \mathbf{q}, \mathbf{b}^{(m)}) \quad (2a)$$

$$w.r.t. \quad \mathbf{v} \quad (2b)$$

$$s.t. \quad \mathcal{M}^{(i)}(\mathbf{v}, \mathbf{b}^{(i)} \mathbf{b}^{(i-1)}) = 0, \quad (2c)$$

$$\mathcal{R}(\mathbf{v}, \mathbf{q}, \mathbf{b}^{(m)}) = 0, \quad i = 1, 2, \dots, m \quad (2d)$$

where  $\mathcal{J}$  is the objective function,  $\mathbf{v}$  are the design variables,  $\mathbf{b}^{(i)}$  are the volume control-point coordinates at mesh movement increment  $i$ , and  $\mathcal{M}^{(i)}$  are the mesh residuals. The Lagrangian function is introduced:

$$\mathcal{L} \equiv \mathcal{J} + \mathbf{\Lambda}^T \mathbf{c} \quad (3)$$

where  $\mathbf{\Lambda}^T = \{\boldsymbol{\lambda}^{(i)}, \boldsymbol{\psi}\}_{i=1}^m$  are the Lagrange multipliers, also called the adjoint variables. Applying the Karush-Kuhn-Tucker (KKT) conditions<sup>21</sup> gives the flow adjoint and mesh adjoint equations, which are then solved for  $\boldsymbol{\psi}$  and  $\boldsymbol{\lambda}^{(i)}$ . The flow adjoint system is solved using GCROT( $m, k$ ), a flexible and modified version of the GCROT method.<sup>22</sup> The mesh adjoint system is solved using the preconditioned conjugate gradient method.<sup>14</sup> Once the Lagrange multipliers are known, the third KKT condition allows for the objective gradient calculation:

$$\mathcal{G} = \frac{\partial \mathcal{J}}{\partial \mathbf{v}} + \sum_{i=1}^m \boldsymbol{\lambda}^{(i)T} \frac{\partial \mathcal{M}^{(i)}}{\partial \mathbf{v}} + \boldsymbol{\psi}^T \frac{\partial \mathcal{R}}{\partial \mathbf{v}}. \quad (4)$$

SNOPT (Sparse Nonlinear OPTimizer),<sup>23</sup> a sparse sequential quadratic programming algorithm, is used to solve the constrained optimization problem. In the problems presented in this paper, the drag force is given as the objective function, while lift, pitching moment, and volume are specified as nonlinear constraints. The gradient evaluation procedure is carried out for the objective and each nonlinear constraint at every design iteration. SNOPT takes the functional values and their gradients and approximates the Hessian using a limited-memory quasi-Newton method. Linear constraints on the geometry are also provided to SNOPT and are satisfied exactly throughout the optimization.

## III. Results

### A. CRM Wing Optimization with Different Thickness Constraints

In the benchmark problem, the twist and section shapes of the CRM wing-only geometry are optimized for drag around a nominal operating point at Mach 0.85 and a Reynolds number of 5 million. There is a lift coefficient constraint  $C_L = 0.50$  and a pitching moment constraint  $C_M \geq -0.17$ . In both the single and multi-point optimizations, the optimizer is able to exploit the minimum 25% thickness constraint to produce very thin outboard sections as well as sharp leading edges.<sup>9</sup> To study the impact of varying the thickness constraints, optimization is re-run with a 75% minimum thickness constraint and a 100% minimum thickness constraint. Table 1 shows the information on the two grid levels used, with the ‘Coarse’ level being used for optimization. The off-wall spacing is given in terms of reference units, which in this case is the mean aerodynamic chord (MAC) of 275.8 inches. The design variables are the  $z$ -coordinates of the B-spline points at 15 spanwise design sections, each with 17 chordwise control points on both the upper and lower surfaces.

Figure 1 shows the optimization convergence histories and Table 2 shows the drag counts of the various optimized geometries, computed on the ‘Fine’ mesh. Figure 2 shows the various optimized geometries and pressure distributions. All of the optimizations are able to reduce the drag and remove the shock near the root, with the main difference in pressure distributions being at the outboard sections. In addition, the thickening of the root section is less pronounced as the thickness constraint increases due to the optimizer’s reduced freedom in redistributing the wing volume. Not surprisingly, the optimized geometry with the lowest thickness constraint has the thinnest airfoil sections and the best drag performance. There is a difference of only 1.5 drag counts between the 75% optimized and the 25% optimized geometry, meaning that the unusually thin sections in the original optimization have a small impact on the overall drag. The wing optimized at 100% thickness is about 5 drag counts higher than the 25% thickness, which is similar to the results of Lyu et al.<sup>24</sup>

Table 1: Grid parameters for CRM wing grid study

Grid	Nodes	Blocks	Off-wall Spacing (ref. units)	$y^+$
Coarse	925,888	40	$1.5 \times 10^{-6}$	0.33
Fine	7,407,104	320	$8.1 \times 10^{-7}$	0.17

Table 2: Results for CRM wing single-point optimization with different thicknesses

	$C_D$ (counts)	$C_M$
Baseline	201.5	-0.1747
25% minimum thickness	185.2	-0.1702
75% minimum thickness	186.7	-0.1708
100% minimum thickness	191.0	-0.1725

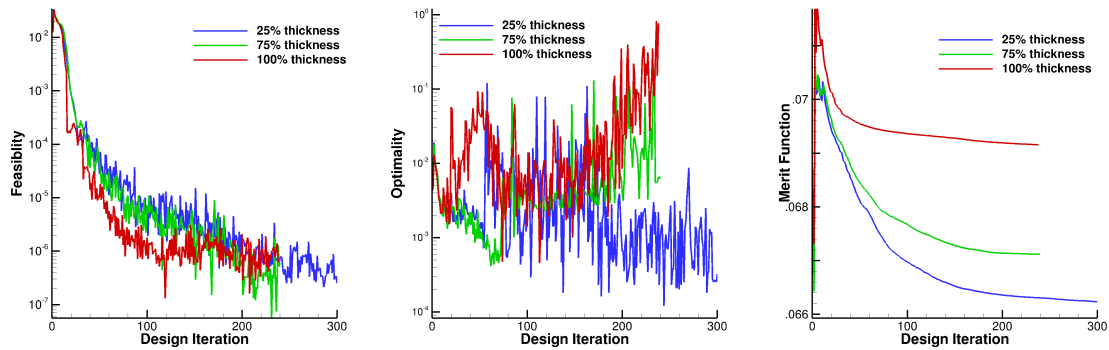


Figure 1: Optimization convergence for varying thickness constraints

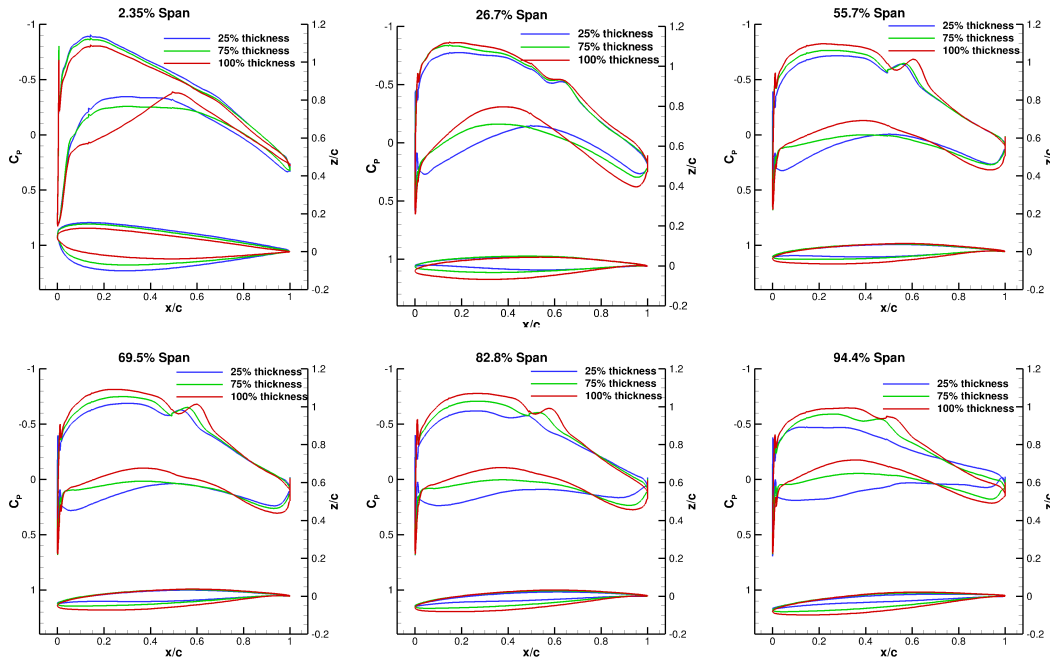


Figure 2: Sectional pressure plots and sections for optimized CRM wings with different thickness constraints, computed on fine mesh

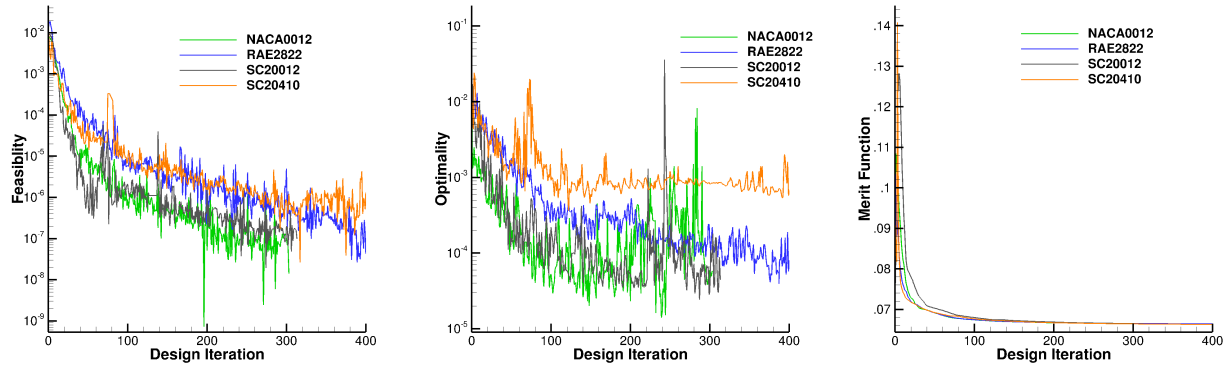


Figure 3: Optimization convergence for CRM optimization with different initial geometries

Table 3: Results for CRM wing single-point optimization with different initial geometries, with drag coefficient computed on coarse optimization mesh

	$C_D$ (counts)	$C_M$
Baseline	218.3	-0.1712
Optimized original geometry	194.5	-0.1700
Optimized with NACA0012 sections	195.2	-0.1700
Optimized with RAE2822 sections	195.0	-0.1700
Optimized with SC20012 sections	195.0	-0.1700
Optimized with SC20410 sections	194.5	-0.1700

## B. CRM Wing Multimodality Investigation

While earlier work by Osusky et al.<sup>25</sup> suggested that the optimization of the CRM wing was a multi-modal problem, difficulties with converging the optimization meant that the solutions obtained were not necessarily local minima. A multimodality study is presented here, using the the single-point CRM optimization and a 25% minimum thickness constraint. The optimized geometries and  $C_D$  values are compared on the coarse optimization mesh. A series of different initial geometries were generated by first creating a control mesh of the original CRM surface, and then replacing the B-spline curve at each spanwise section with the B-spline curve of a specified airfoil section, scaled with the correct chord and twist. The geometric constraints such as volume and thickness are still based on those of the original CRM wing geometry. The initial airfoils used include the NACA0012, RAE2822, SC20012 and SC20410 sections.

Table 3 summarizes the optimized drag coefficients evaluated at  $C_L = 0.50$ , and Figure 4 shows the optimized sections and pressure distributions. All of the optimized geometries are within one drag count of the original single-point optimization and the section shapes are nearly the same. Figure 3 shows the convergence histories for the different optimizations. All of the optimizations were able to run for over 350 design iterations until the there was no longer any significant change in drag. With the exception of the case beginning with SC20410 sections, all the cases reduced the optimality by around two orders of magnitude, indicating that they are fairly close to the optimum. In Figure 4, the SC20410 optimization shows a significant deviation in sectional shape from the rest of the geometries at 55.7% span. Since this is the also the case with the least optimality reduction in optimality, it is likely that running this optimization for longer will lead to the same geometry. The similarities in the section shapes suggest that the CRM wing optimization does not have multiple local optimum solutions. While this conclusion contrasts that of Osusky et al.,<sup>25</sup> the improved optimality reductions here make these results more definitive.

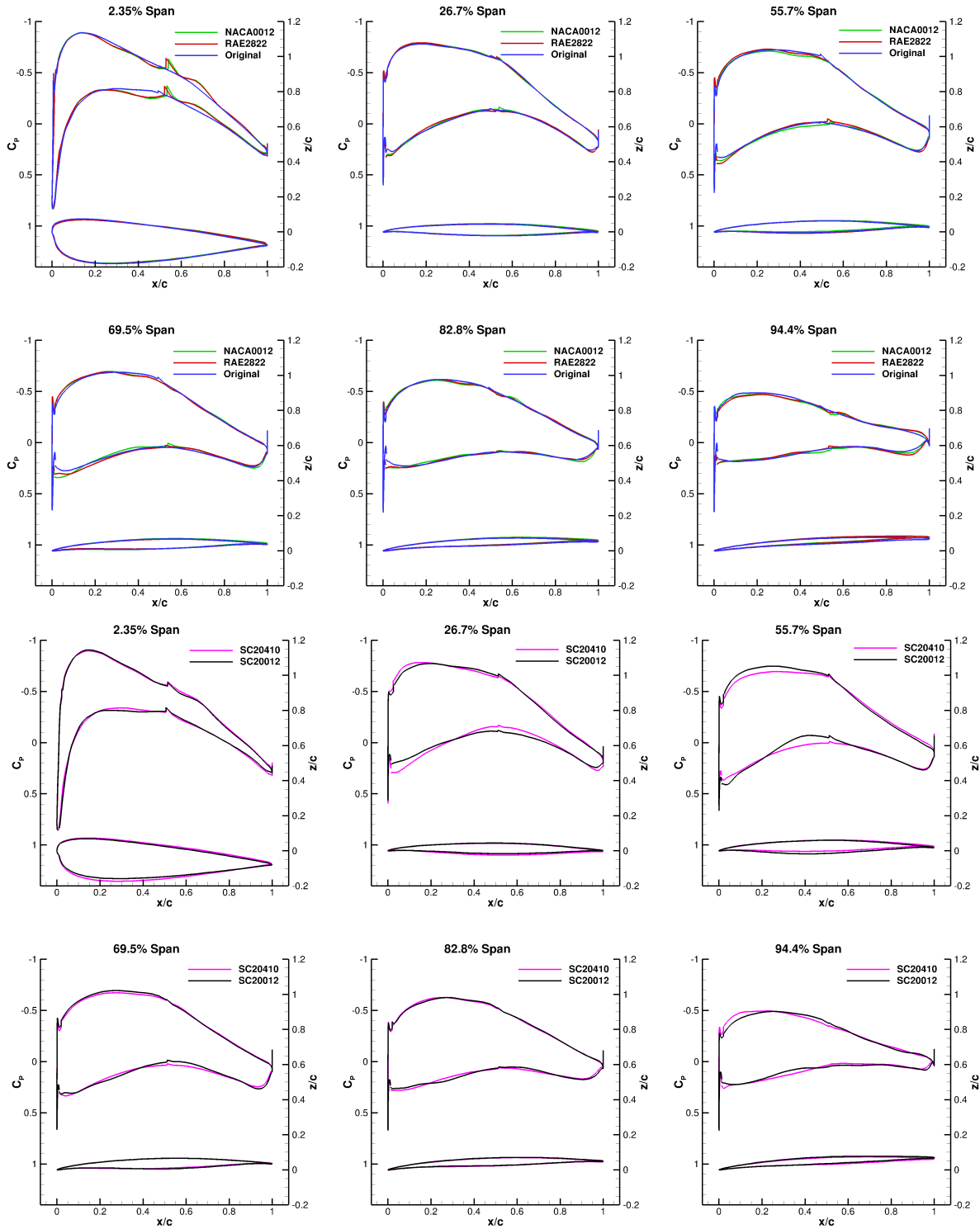


Figure 4: Sectional pressure plots and sections for optimized CRM wings with different initial geometries, computed on the optimization mesh

**Table 4: Grid parameters for CRM wing-body-tail**

Grid	Nodes	Blocks	Off-wall Spacing (ref. units)	$y^+$
Coarse	5,393,750	278	$9.2 \times 10^{-7}$	1.02
Fine	43,150,000	2224	$5.2 \times 10^{-7}$	0.52

**Table 5: Results for CRM wing-body-tail single-point optimization**

	Optimization Mesh		Fine Mesh		Tail Angle
	$C_D$ (counts)	$C_M$	$C_D$ (counts)	$C_M$	
Baseline	282.5	-0.047	235.4	-0.048	0°
Optimized	271.3	0.000	230.3	0.003	-1.08°

### C. CRM Wing-Body-Tail

#### *Optimization Problem*

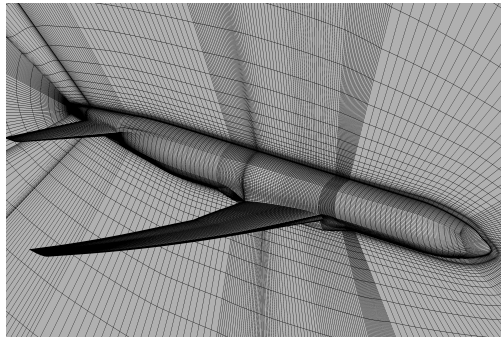
Case 5 of the ADODG benchmark cases<sup>b</sup> is an extension of the previous CRM problem to include fuselage effects and trim constraints into the optimization.<sup>2</sup> A single-point lift and trim constrained drag minimization is performed on the full CRM Wing-Body-Tail configuration from the Fifth AIAA Drag Prediction Workshop. As with the previous case, the geometry is optimized at  $M = 0.85$  and  $C_L = 0.5$ , this time with a more realistic flight Reynolds number of 43 million. The main design variables are the wing section shape and twist, this time subject to a minimum 100% thickness constraint. A trim constant, i.e.  $C_M = 0$ , is enforced at the moment reference location at (1325, 0, 177.95) inches. Finally, the horizontal tail is free to rotate to adjust the moment.

Table 4 shows the grid parameters for the O-O mesh, which was generated in ICEM CFD. The off-wall spacing is given in reference units, based on the same MAC as the wing-only case of 275.8 inches. Figure 5 shows the computational mesh, as well as the FFD parameterization. The wing is embedded into an FFD volume composed of 17 design sections, each with 17 FFD chordwise control points on the upper and lower surface.<sup>9</sup> This approach is particularly advantageous in the case of a wing-body optimization as the wing-fuselage interface geometry can also be embedded within the FFD volume, allowing the geometry at the junction to flexibly conform to changes in the root wing section. The FFD lattice points on the horizontal tail are not used as design variables; rather the rotation angle of the tail FFD volume about the reference point is the design variable. Combined with the angle of attack, there are a total of 580 design variables.

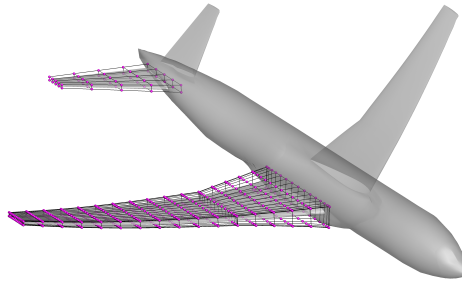
#### *Results*

The optimization was run for approximately 144 hours, using 278 processors. Table 5 summarizes the initial and optimized drag coefficients and moment coefficients. All values are computed using a reference area of 594,720 in<sup>2</sup>. The optimization has reduced the drag by 11 counts on the coarse mesh, which translates to a difference of 5 counts when analyzed on the fine mesh. Note that on the fine mesh, the aircraft still has a slight pitching moment. Figure 6 shows the initial and optimized pressure contours, as well as the convergence history. The feasibility is reduced by several orders of magnitude as the optimizer trims the aircraft at the desired lift coefficient. The optimality is reduced by about one order of magnitude. Figure 7 shows the sectional pressure coefficient plots and shapes. The plot at  $y/b = 0.5024$  shows that the optimizer is successful in eliminating the shock and smoothing out the pressure recovery. The optimizer rotates the tail down one degree and reduces the overall drag by 2% relative to the baseline untrimmed geometry, a result which agrees well with Chen et al.<sup>2</sup>

<sup>b</sup><https://info.aiaa.org/tac/ASG/APATC/AeroDesignOpt-DG/>



(a) CFD Mesh



(b) B-spline Surface

Figure 5: The computational mesh and FFD parameterization for the CRM wing-body-tail geometry

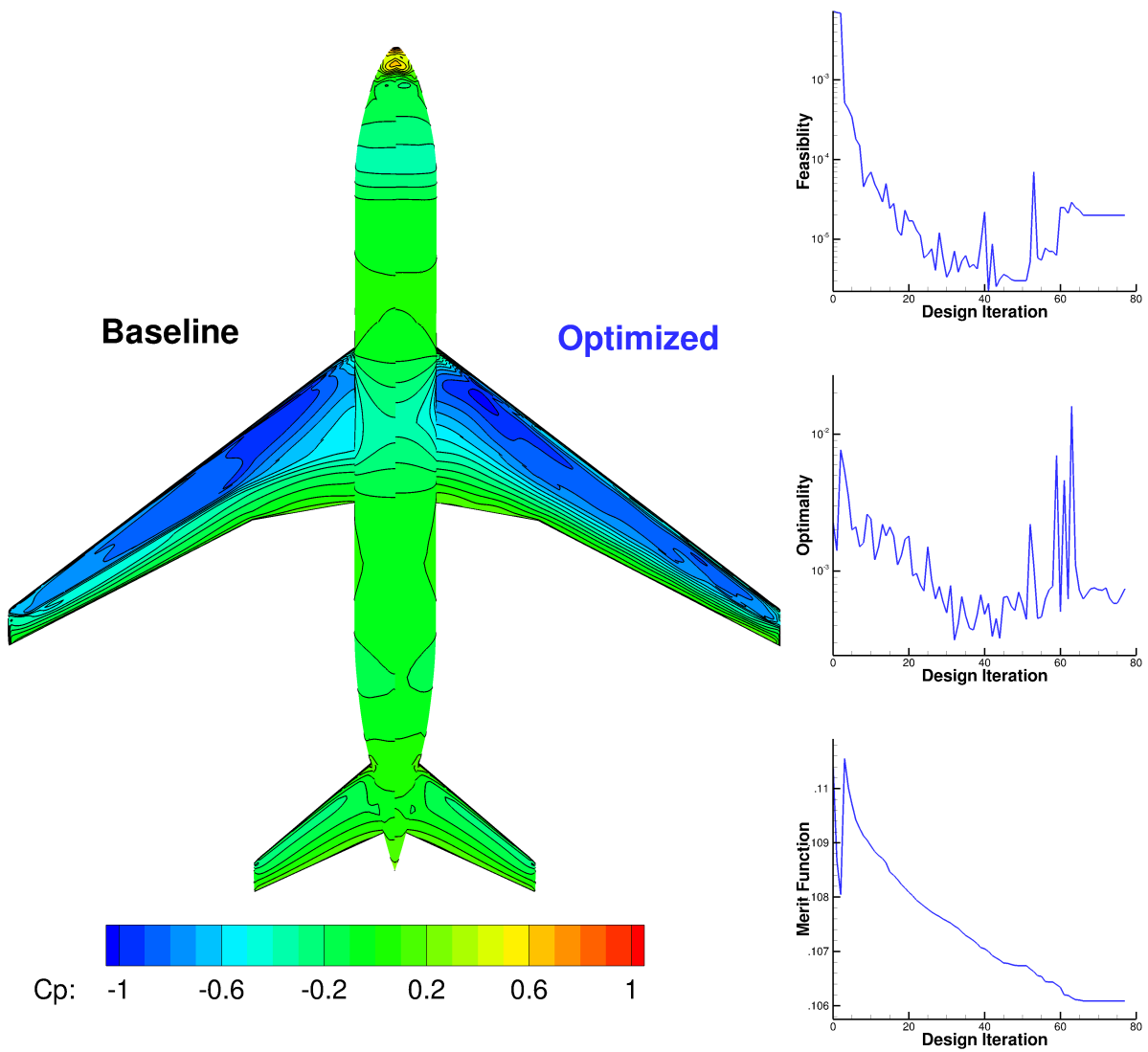


Figure 6: Initial and optimized surface contours for CRM wing-body-tail configuration, as well as optimization convergence

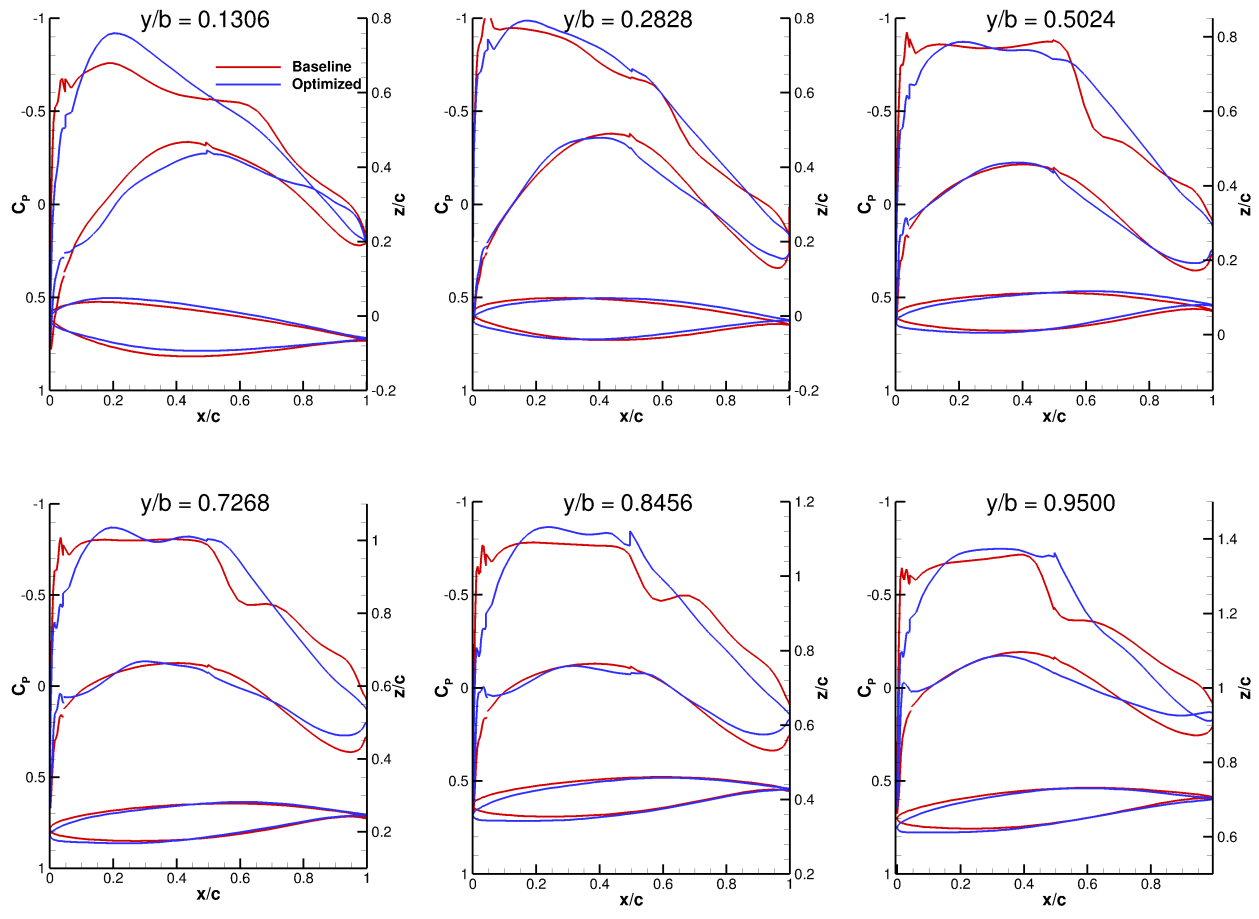


Figure 7: Sectional pressure plots and sections for optimized CRM wing at  $C_L = 0.5$  and a Mach number of 0.85

**Table 6: RAE 2822 Optimization - multi-point operating points**

Point $i$	Weight $\mathcal{T}_i$	$M$	$C_l$	$Re$
1	1.0	0.734	0.504	$6.50 \times 10^6$
2	1.0	0.734	0.704	$6.50 \times 10^6$
3	1.0	0.734	0.804	$6.50 \times 10^6$
4	1.0	0.734	0.824	$6.50 \times 10^6$
5	0.5	0.734	0.844	$6.50 \times 10^6$
6	0.5	0.714	0.844	$6.50 \times 10^6$
7	0.5	0.744	0.804	$6.50 \times 10^6$
8	0.5	0.650	0.804	$6.50 \times 10^6$

**Table 7: Grid parameters for RAE 2822 multi-point optimization**

Grid	Nodes (2D)	Off-wall Spacing (ref. units)	$y^+$
Coarse	47,824	$3.7 \times 10^{-6}$	0.82
Medium	187,792	$1.8 \times 10^{-6}$	0.39
Fine	748,064	$8.7 \times 10^{-7}$	0.15

## D. RAE 2822 Airfoil Multi-point Optimization

### *Optimization Problem*

Case 2 of the benchmark ADODG problems is the single-point drag minimization of the RAE 2822 airfoil in transonic, viscous flow. Results from Lee et al.<sup>9</sup> and Ledoux et al.<sup>26</sup> showed that geometries optimized for this problem can have non-unique flow solutions and poor off-design behaviour. A multi-point optimization is presented here for in an attempt to produce more robust airfoils.<sup>27</sup> Table 6 lists the operating points, with the nominal operating point at  $M = 0.734$  and  $C_l = 0.824$ . Table 7 shows the grid parameters for this case, which uses a C-grid topology. The ‘Coarse’ level is used for optimization, while the ‘Fine’ mesh level is used to compute the drag coefficients and drag polars. The design variables are the  $z$ -coordinates of 34 B-spline surface points making up the airfoil top and bottom surfaces.<sup>9</sup> The airfoil must maintain the same cross-sectional area as the original RAE 2822 airfoil. Additional thickness constraints are enforced near the trailing edge to prevent unrealistically thin geometries.

### *Results*

The eighth operating point presented the most difficulty for the optimizer, as the low-speed lift constraint requires a high angle of attack. Figure 8 shows that Jetstream is able to reduce the optimality measure by nearly two orders of magnitude despite the difficulty at this operating point. Figure 9 shows the optimized airfoil and pressure distribution at the nominal operating condition, compared to the baseline RAE 2822 airfoil and the single-point result from Lee et al.<sup>9</sup> The multi-point airfoil shows a rounder leading edge and less camber than the single-point results, which is due to the presence of the low-speed lift constraint. While both optimizations remove the shock at the nominal operating condition, the multi-point airfoil has a bump in the pressure recovery which hurts its performance slightly. The drag polar in Figure 10, computed on the fine mesh, shows that the multi-point result has a much better behaviour at off-design points and does not have the sharp drag cliff from the single-point airfoil.

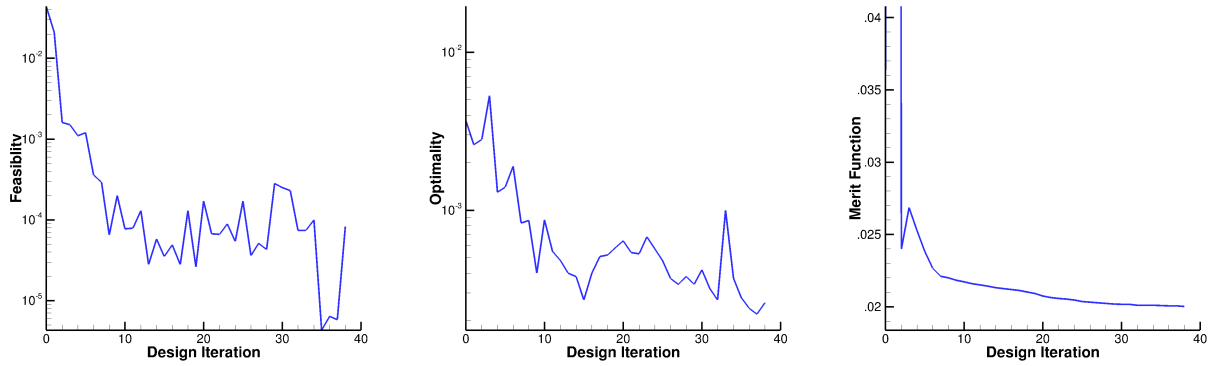


Figure 8: Optimization convergence for RAE 2822 multi-point optimization

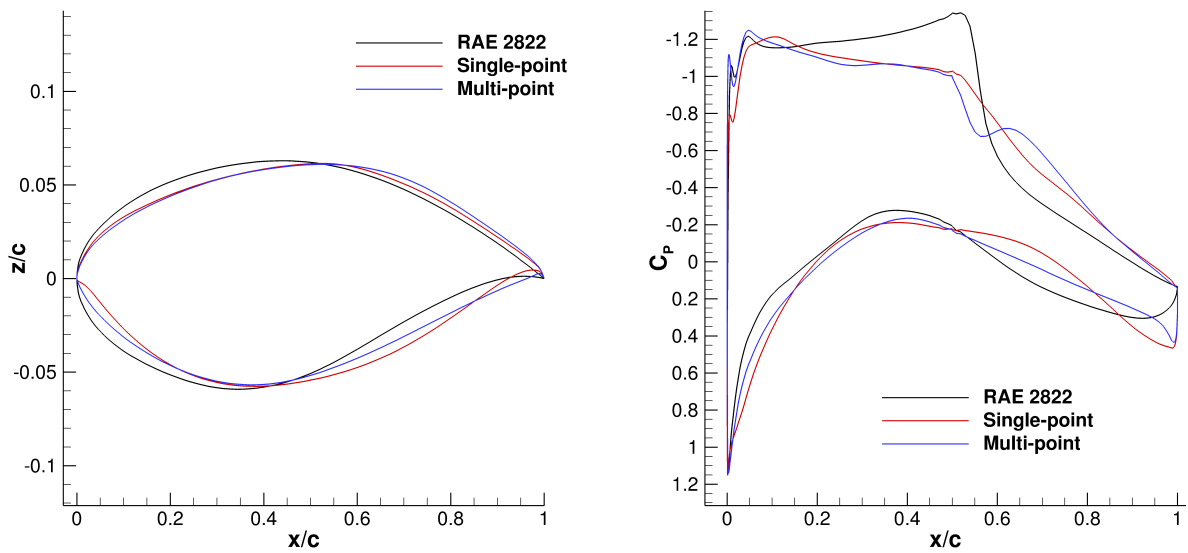


Figure 9: RAE 2822 multi-point optimization - airfoil shapes and pressure distribution at  $M = 0.734$ ,  $C_L = 0.824$

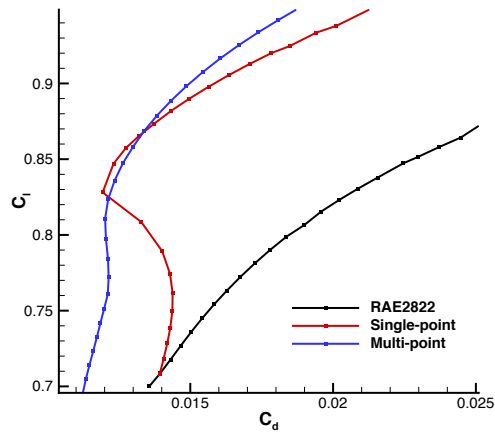


Figure 10: RAE 2822 multi-point optimization - drag polar at Mach 0.734, computed on the fine mesh

**Table 8: RAE 2822 Optimization - Off-design constraints**

Point $i$	$Re$	$M$	$C_l$	Constraint
1	$30.45 \times 10^6$	0.80	0.30	$M_{max} \leq 1.35$
2	$30.45 \times 10^6$	0.80	0.16	$M_{max} \leq 1.35$
3	$30.45 \times 10^6$	0.80	0.47	$M_{max} \leq 1.35$
4	$30.45 \times 10^6$	0.80	0.26	$M_{max} \leq 1.35$
5	$21.39 \times 10^6$	0.80	0.48	$M_{max} \leq 1.35$
6	$21.39 \times 10^6$	0.80	0.26	$M_{max} \leq 1.35$
7	$21.39 \times 10^6$	0.80	0.76	$M_{max} \leq 1.35$
8	$21.39 \times 10^6$	0.80	0.41	$M_{max} \leq 1.35$
9	$11.80 \times 10^6$	0.16	1.60	$C_{lmax} \geq 1.60$
10	$15.00 \times 10^6$	0.20	1.60	$C_{lmax} \geq 1.60$

### Optimization Problem 2

A second problem is presented as an alternative for the multi-point optimization of the RAE 2822. This problem, first studied by Buckley and Zingg,<sup>28</sup> is based on the hypothetical design of a transonic civil transport aircraft. The objective is to minimize the integral of  $C_d$  over a range of operating conditions. The aircraft weight ranges from 100,000 to 160,000 lbs at a cruise altitude of 39,000 ft. The cruise Mach number ranges from 0.88 to 0.94, but with sweep taken into account, the effective Mach number range for the airfoil is from 0.72 to 0.77. The Reynolds number is 19.2 million for  $M = 0.72$ , and is adjusted for each Mach number. The integral for the objective function is defined as

$$\int_{W_1}^{W_2} \int_{M_1}^{M_2} C_d(M, W) dM dW. \quad (5)$$

This objective function can then be formulated as an approximation of this integral using a quadrature rule, which gives the following:

$$\sum_{i=1}^{N_M} \sum_{j=1}^{N_W} \mathcal{T}_{i,j} C_d(M_i, W_j) \Delta M \Delta W, \quad (6)$$

where  $N_M, N_W$  are the number of quadrature points used,  $\Delta M, \Delta W$  are the spacings between points, and  $\mathcal{T}_{i,j}$  are the quadrature weights to approximate the integral. In our results, the integral is approximated using five points in both Mach number and weight, and a trapezoidal quadrature rule ( $\mathcal{T} = [\frac{1}{2}, 1, \dots, 1, \frac{1}{2}]$ ). The design variables and geometric constraints are identical to the previous multi-point case. The grid is the same as the previous problem, with a slight change in the off-wall spacing for the higher Reynolds numbers. In addition to optimizing over the range of operating conditions, a ten off-design constraints are specified, shown in Table 8. The first eight are specified to reduce shock strength and maintain maneuverability at dive conditions, while the last two constraints are low-speed lift requirements.<sup>29</sup> The choice of  $C_{l,max} = 1.6$  accounts for the coarse optimization mesh. It is expected that the  $C_{l,max}$  computed on a fine mesh will be significantly higher.<sup>28</sup> The maximum Mach number constraints are enforced using Kreisselmeier-Steinhauser (KS) aggregation functions.<sup>30</sup>

### Results

The RAE 2822 airfoil was first optimized without the off-design constraints. The resulting geometry was then used as an input into an optimization run which included the constraints in Table 8. Figure 11 shows the optimized airfoils and  $C_d$  vs. Mach number plot for the RAE 2822 and optimized airfoils. The flow solution for each geometry is computed on a fine mesh at different aircraft weights and Mach numbers within the design range. For each Mach number, the drag coefficient is integrated over the weight and the result is divided by the range of aircraft weights to compute the average  $C_D$ , plotted in Figure 11. As expected, there is a significant performance penalty when including the off-design performance constraints. The maximum Mach number constraints cause the off-design optimized airfoil to have a flatter upper surface. The addition

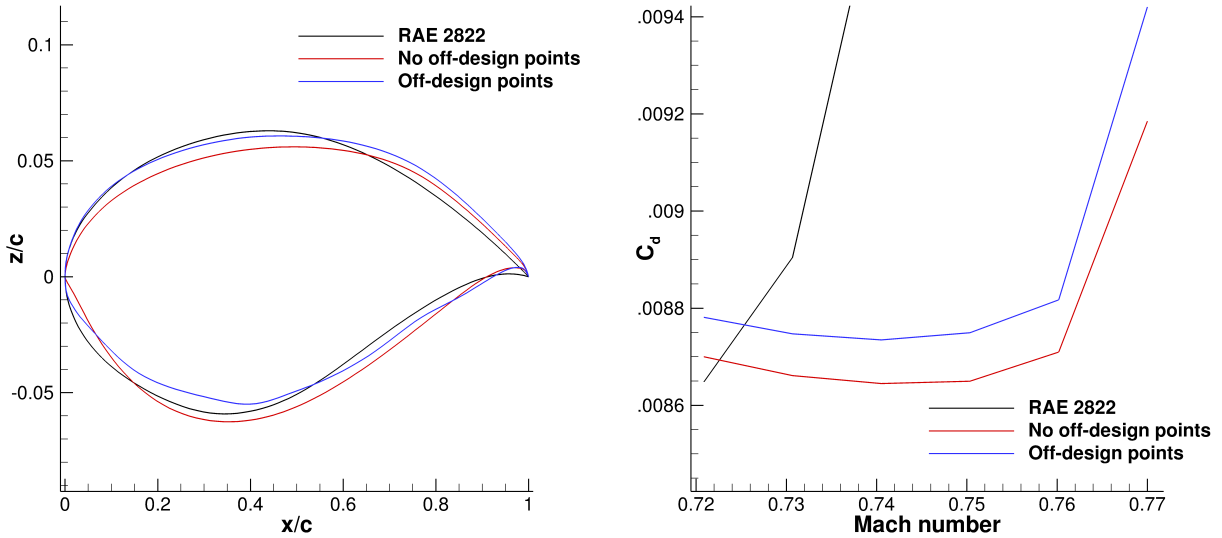


Figure 11: RAE 2822 multi-point optimization problem 2 - airfoil shapes and average  $C_d$  vs. Mach number

of low-speed lift constraints cause the optimizer to produce a more rounded leading edge. The results here are somewhat different than those obtained by Buckley and Zingg,<sup>28</sup> and work is underway to determine the cause.

## E. Planform Optimization

### *Optimization Problem*

The goal of this optimization is to demonstrate Jetstream’s ability to produce large changes in both wing planform and section shape during optimization. The initial wing is rectangular with NACA0012 sections. Jetstream is tasked with turning this poorly designed wing into one suitable for transonic flight. The initial chord is used as the reference length and the initial span is 3.0 reference units. The design variables enabled are wing sweep, wing span, taper, section shape, twist and angle of attack. The projected area of the wing  $S$  is free to change, as long as the optimizer achieves a non-dimensionalized lift of  $C_L S = 2.0$ . The limits on these planform variables, shown in Table 9, are chosen so that they allow for significant planform change but are somewhat realistic. Nevertheless, this is intended as a problem for testing the methodology, not a practical design study. In addition, the following constraints are imposed:

- The wing maintains at least 85% of its original thickness at any location;
- the wing volume must be greater than or equal to its original volume;
- the root bending moment must be less than or equal to that of an elliptical wing of with a half-span of 4.0 reference units..

Table 10 lists some of the statistics for the O-O grid used in this optimization. The wing consists of 32 surface patches fitted with  $9 \times 9$  B spline control points. The wing surface is then embedded into an FFD volume with 10 spanwise control sections and 10 chordwise control points. Figure 12 shows the computational mesh and the FFD setup for this optimization. The FFD volume is in turn driven by a simple linear axial curve which can control the wing’s span and sweep. The wing geometry has an initial volume of  $V = 0.24$  cubed reference units and a reference area of  $S = 3.0$  squared reference units. The flow analysis is performed at a Reynolds number of  $20 \times 10^6$  and at both Mach 0.78 and Mach 0.85. Despite the fact that the wing chords are free to change, the final geometries are tapered such that the overall mean aerodynamic chord is close to one, meaning that the initial Reynolds number is still valid at the end of optimization.

**Table 9: Planform variable limits**

Variable	Units	Upper	Lower
Half-Span	ref. units	3.95	1.00
Chord	ref. units	2.0	0.1
Taper	ratio	20.0	0.10
Tip Twist	degrees	4.0	-4.0
Quarter Chord Sweep	degrees	32.0	-32.0
Angle of Attack	degrees	-4.0	4.0

**Table 10: Grid parameters for planform optimization**

Grid Level	Nodes	Blocks	Off-wall Spacing (ref. units)	Average $y^+$
Coarse	1,320,000	64	$1.35 \times 10^{-6}$	0.75
Fine	10,560,000	512	$7.30 \times 10^{-7}$	0.32

**Table 11: Results summary**

	Mach 0.78	Mach 0.85
$C_L$	0.608	0.563
$S$ (ref.units <sup>2</sup> )	3.29	3.55
$C_{DS}$	0.0682	0.0727
$C_D$ (counts)	207	205
$L/D$	29.3	27.5
$\alpha$	3.19°	2.83°
Span (ref. units)	3.95	3.95
Root Chord (ref. units)	1.42	1.36
Taper Ratio	0.17	0.32
Sweep	32.0°	32.0°

## Results

Figure 13 shows the optimization convergence history - both optimization cases are able to run without error for over 200 iterations and achieve about three orders of magnitude reduction in optimality. Table 11 summarizes the results of the optimizations performed at both Mach numbers. The thickness, volume, and root bending moment constraints are active at convergence in both optimizations. Figure 14 shows the initial solution on the NACA0012 at Mach 0.85 at  $\alpha = 2.0^\circ$ , displaying a strong shock on the upper surface of the wing. The optimizer is able to produce large changes in both the planform as well as the airfoil. The drag values are computed on the fine mesh level. Of the planform variables, only the span and sweep variables are at their upper limit, the former to minimize induced drag and the latter to reduce wave drag.

In each case, the taper of the wing is used to adjust to the optimal planform area. At the higher Mach number of 0.85, the optimizer creates a larger wing area to reduce the lift coefficient, reducing wave drag at the cost of increasing friction drag. The section shapes show significant change from the initial NACA0012 airfoil and are all free of strong shocks. The sections optimized for Mach 0.85 also have a flatter upper surface and aft camber than those optimized at Mach 0.78. Figures 15 and 16 show the optimized planform geometries, pressure contours, as well as section data at various spanwise locations for the optimized wings, all computed on the fine mesh level. An oscillation in the pressure distribution appears near the tip in Figure 16 in the fine mesh analysis, which was not apparent in the coarse mesh optimized surface. Running the optimization at a finer mesh level would likely remove this feature. The results of this case are a stiff test of the aerodynamic optimization methodology, especially of the ability to handle large shape changes.

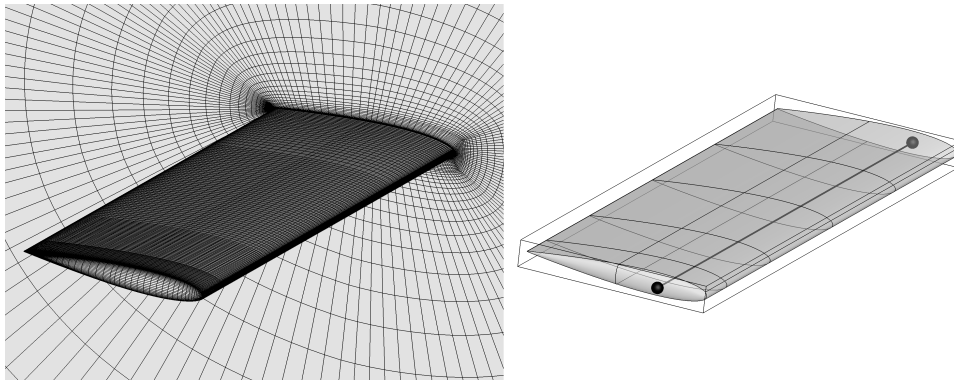


Figure 12: Initial mesh and FFD parameterization for planform optimization

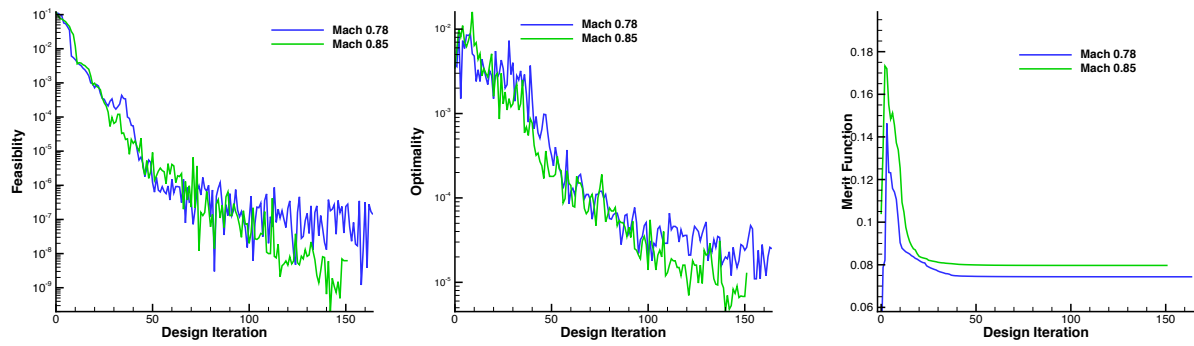


Figure 13: Optimization convergence for planform optimization

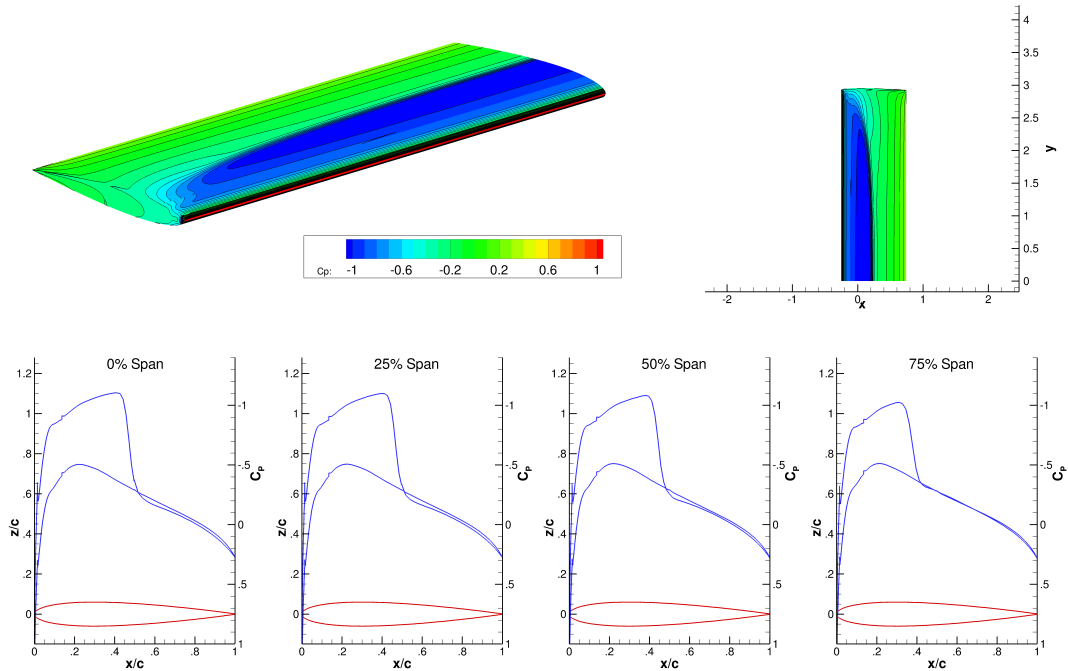


Figure 14: Initial flow solution on the rectangular NACA0012 wing at Mach 0.85, computed on the fine mesh

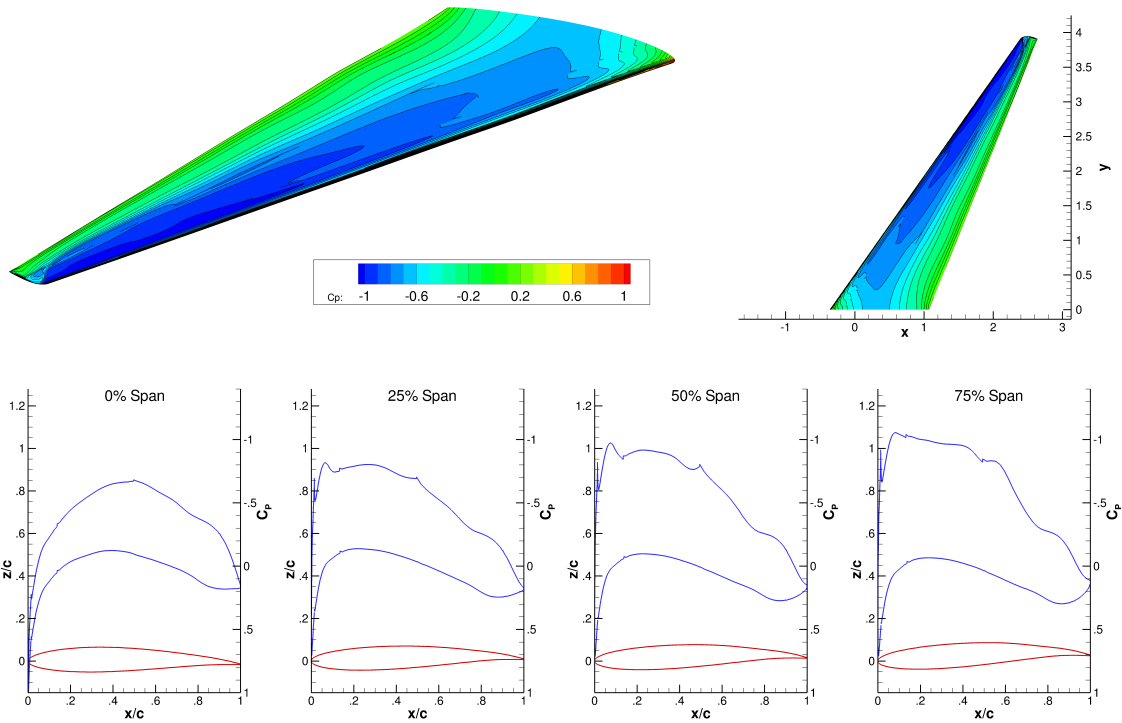


Figure 15: Optimized planform and section geometry and pressure contours at Mach 0.78, computed on the fine mesh

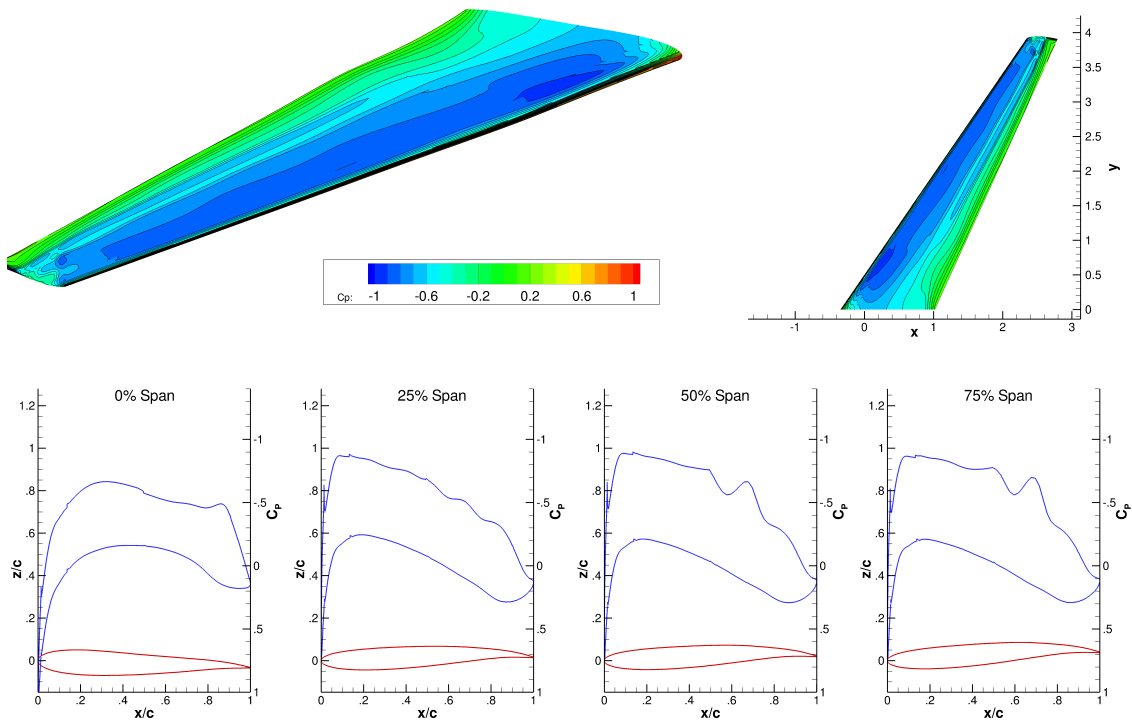


Figure 16: Optimized planform and section geometry and pressure contours at Mach 0.85, computed on the fine mesh

Table 12: Grid parameters for the wing based on the Boeing 737-900

Grid Level	Blocks	Nodes	Off-wall Spacing (ref. units)	Average $y^+$
Coarse	1,631,000	64	$7.8 \times 10^{-7}$	0.45
Fine	13,048,000	512	$3.2 \times 10^{-7}$	0.23

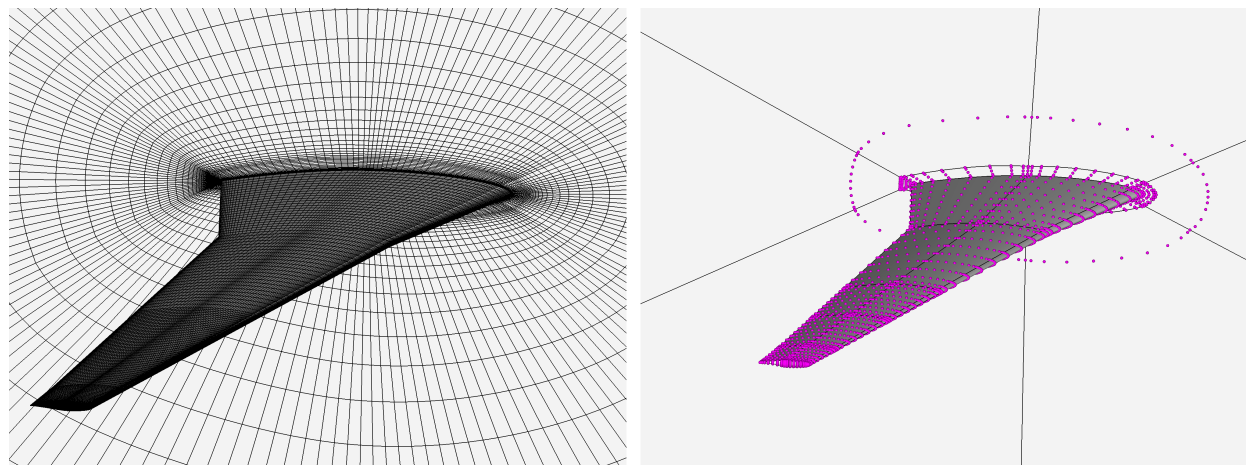


Figure 17: Initial wing - the computational grid (left) and the B-spline control mesh (right)

## F. Wingtip Optimization

### *Optimization Problem*

Hicken and Zingg<sup>31</sup> and Osusky and Zingg<sup>25</sup> worked on winglet design starting from a flat plate for a rectangular NACA0012 in subsonic flow. Here the initial geometry and flow conditions are similar to the inviscid, aerostructural optimization performed by Khosravi and Zingg.<sup>32</sup> The initial wing geometry has a planform based on the Boeing 737-900 with RAE2822 airfoil sections and no initial twist. The optimization is done at a Mach number of 0.78 and a Reynolds number of 20 million. The design variables are the airfoil sections, geometric twist, and the angle of attack. At the wingtip, the taper, sweep, and dihedral are free. In addition to design variable bounds, the following constraints are imposed:

- The wing must maintain at least 75% of its original thickness at any location;
- the initial volume of the wing from root to 90% of the span must be maintained;
- the wing must produce lift equal to the original wing at a  $C_L$  of 0.50;
- the wingtip cannot extend past the span of the initial wing;

The Boeing 737 wing is normalized by using the MAC of 3.96 metres as the reference unit. The initial geometry has a projected area of  $S = 2.899$  squared reference units for the half-wing. The initial volume from the wing root to 90% of the span is  $V = 0.1856$  cubed reference units, and is maintained throughout the optimization to constrain the wing sections from becoming too thin. There is no volume constraint on the wingtip design. Each optimization may alter the projected area as long as it produces a non-dimensionalized lift of  $C_L S = 1.449$ . The overall reduction in drag is computed based on  $C_D S$ .

A series of configurations are optimized, including optimization with only section shape and twist variables, a raked wingtip, and winglet up/down. The cases are optimized on the O-grid outlined in Table 12. The computational mesh is mapped to a control mesh in Figure 17, which is embedded in two axial curve driven FFD volumes. The first FFD volume governs the majority of the wing from the root to 90% of the span; this portion of the wing can optimize section shape and twist but not the planform. The second FFD volume, shown in Figure 18, governs the wingtip; in addition to section and twist, the taper is free and the axial curve control points are allowed to move to adjust sweep and wingtip height. The wingtip axial curve

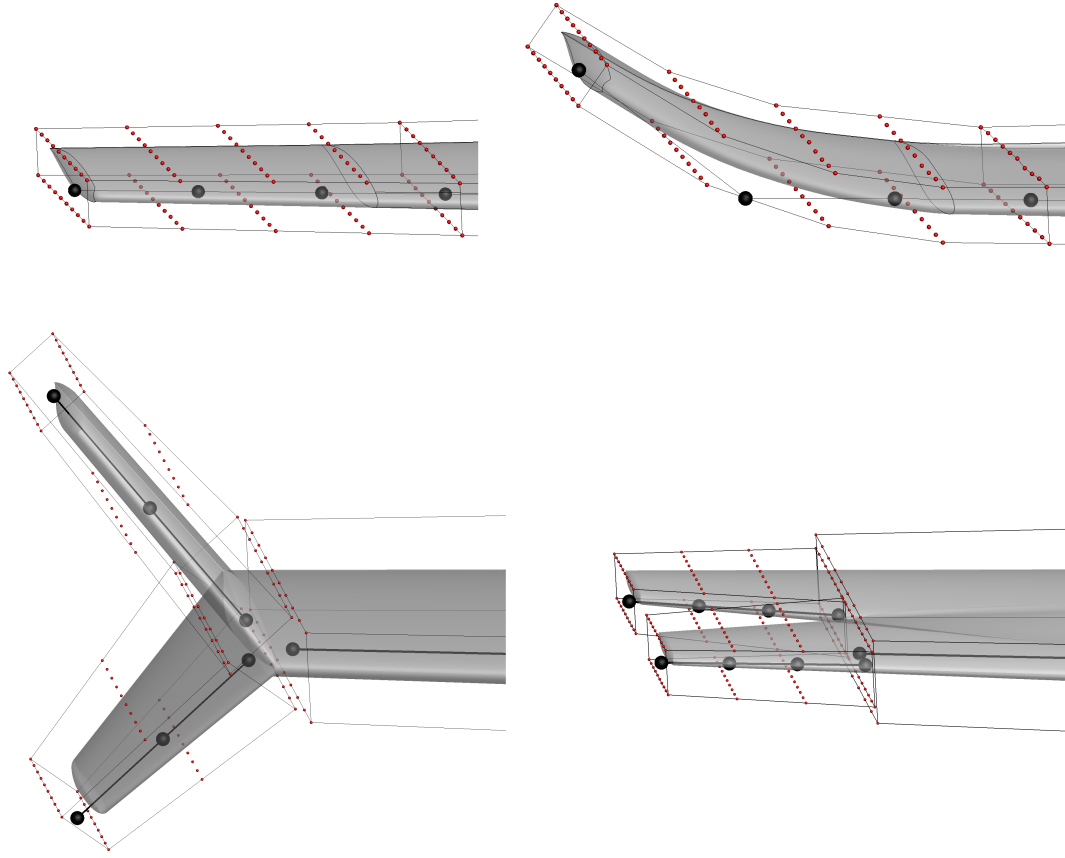


**Figure 18: The FFD parameterization of the wingtip - planar geometry (top left), winglet (top right), wingtip fence (bottom left) and split-tip (bottom right)**

is parameterized with a fourth-order B-spline curve to ensure a smooth blend from the planar wing to the winglet.

In the first case, only the wing section and twist are design variables. In the raked wingtip, the optimizer also designs the wing section and twist, but the wingtip is given the additional freedom to design taper and sweep. In the winglet optimization, the wing has the same degrees of freedom as the raked tip, with the additional freedom for the outermost axial control point to move vertically up or down. The second outermost axial control point has some freedom to move in the spanwise direction to control the radius of curvature of the winglet transition. Finally, all axial control points cannot extend the wing past its original span. The maximum height to span ratio ( $h/b$ ) allowed for each winglet is 10%.

In addition, a wingtip fence and a split-tip configuration are optimized. Due to the complexity of the geometries, these cases are performed on separate grids, each with similar off-wall spacing to that in Table 12. In the wingtip fence, the wingtip is split into two extensions - one up and one down. Each extension is governed by an axial FFD volume and is allowed to change taper, sweep, and height independently. The split-tip is parameterized similarly, with the wingtips split in the chordwise direction. Figure 18 shows the FFD parameterization of both initial geometries. In both cases, the entire wing section and twist are designed while the total span, volume and lift constraints are kept at the same values as in the first four cases. In addition, the maximum distance between the upper and lower wingtip for both cases is restricted to the same maximum  $h/b$  ratio for the winglets.

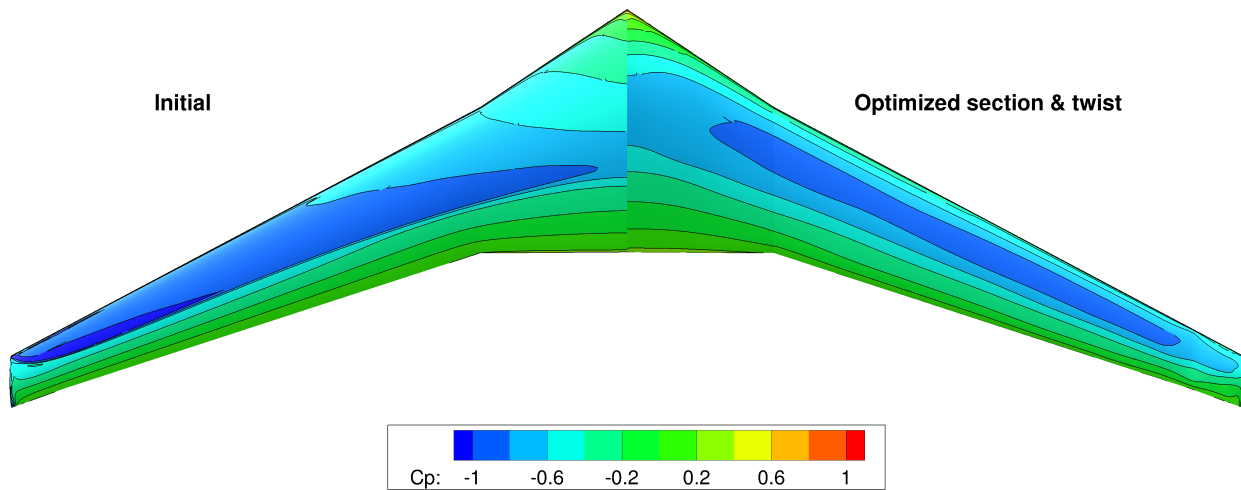


Figure 19: Initial and optimized pressure contours with no wingtip optimization

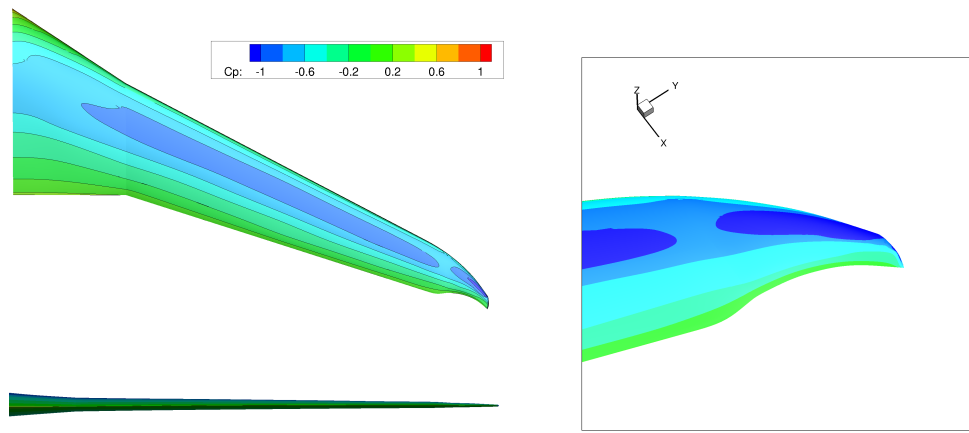
Table 13: Results summary for RANS wingtip optimization

	Initial	Section only	Raked Tip	Winglet Down	Winglet Up	Wingtip Fence	Split-tip
$S$	2.899	2.899	2.848	2.874	2.880	2.889	2.885
$C_L$	0.500	0.500	0.509	0.504	0.503	0.502	0.502
$C_D$ (counts)	171.5	154.9	156.4	151.4	152.8	151.7	156.4
$L/D$	29.15	32.25	32.53	33.29	32.89	33.05	32.09
$\alpha$	2.41°	1.44°	1.57°	1.96°	1.83°	1.98°	1.05°
$C_{D,pressure}$	119.6	101.9	103.4	97.5	98.7	96.8	102.2
$C_{D,friction}$	51.9	53.0	52.9	53.9	54.1	54.9	54.2
$\Delta C_D S$	0.0%	-9.7%	-10.4%	-12.5%	-11.5%	-11.8%	-9.3%

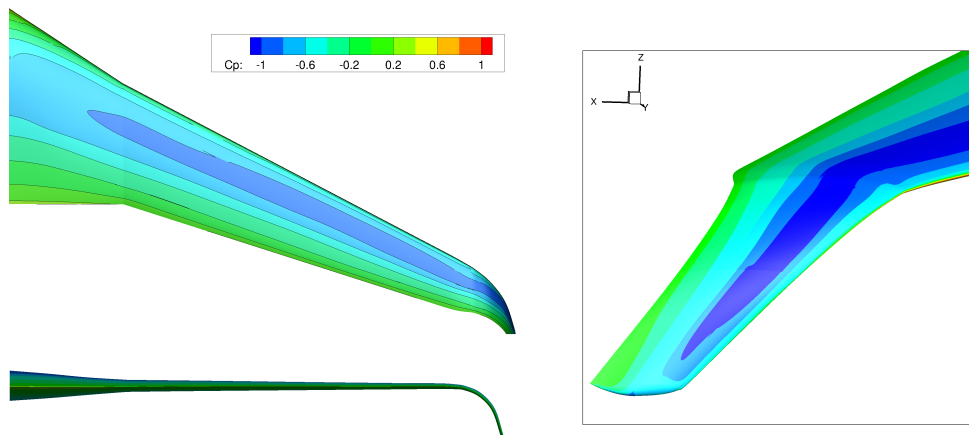
## Results

Table 13 summarizes the optimization results. While the optimizations are performed on the ‘Coarse’ grid level, all of the drag values are computed on the ‘Fine’ grid level, shown in Table 12. Although the optimization meshes for the wingtip fence and split-tip are different than the previous four due to their unique topology, the final drag values are computed on a mesh with around 13 million nodes to provide an accurate comparison to the rest of the geometries. Figure 19 shows the initial wing and the wing with optimized section variables. Figures 20 and 21 show the geometries and pressure contours for the wings with optimized wingtips. All of the optimizations manage to eliminate the shock on the initial geometry and create smoother pressure contours over the wing surface. In the cases with nonplanar geometries, the optimizer is trading off between induced drag and surface friction drag.

In the section optimization, the optimizer adjusts the airfoil section and quarter-chord twist to remove shock and optimize the spanwise lift distribution. In the raked tip, the wingtip is tapered and swept back as far as possible, providing a small improvement. When the optimizer was given the freedom to choose a winglet up or down, it always chose to create a winglet down. As a result, an additional optimization was run with the winglet constrained to only move upwards. The optimized winglet down leads to the greatest improvement in drag, suggesting that even when the wingtip is initially planar, the optimizer can determine immediately that a downward winglet is the optimal solution. In both the winglet up and down



(a) Optimized raked wingtip

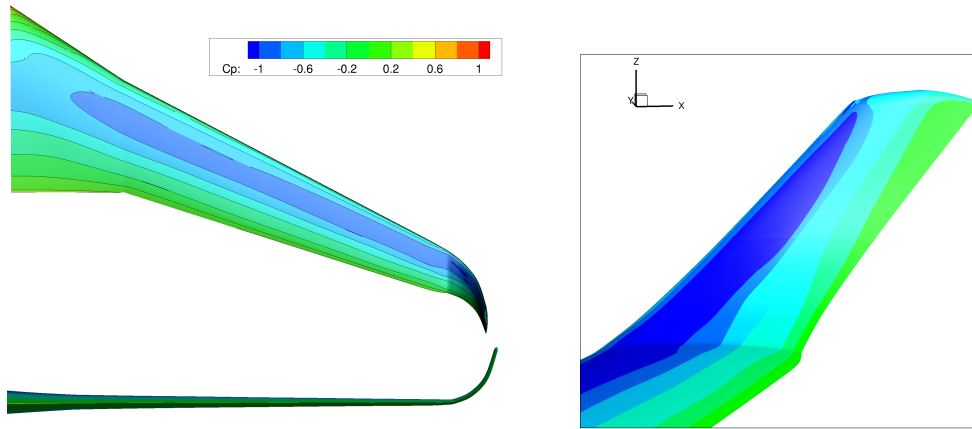


(b) Optimized winglet down

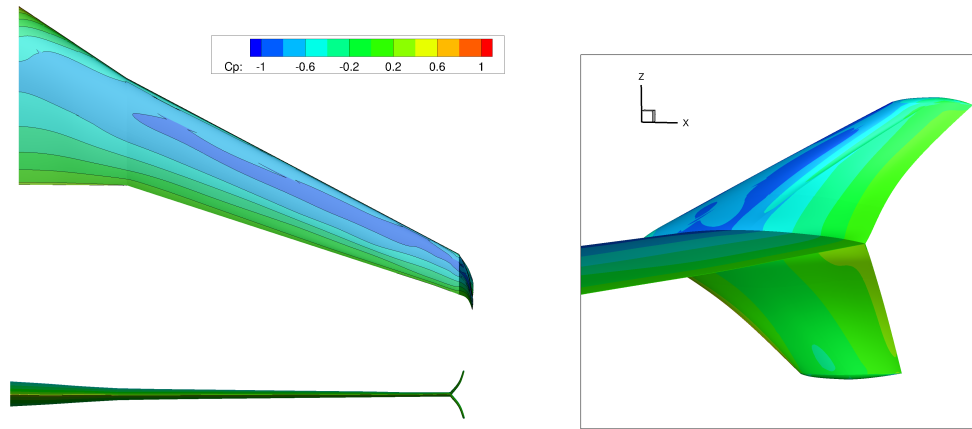
**Figure 20: Optimized geometries and wingtips for raked and winglet down configurations**

configurations, the optimizer designs the winglet to reach the maximum  $h/b$ , suggesting that large winglets are beneficial despite the increase in wetted area. Both winglets are swept back as far as possible; the winglet down has washout while the winglet up has wash-in. Despite the formation of a winglet, the optimizer tapered the wingtip sections to decrease the projected area.

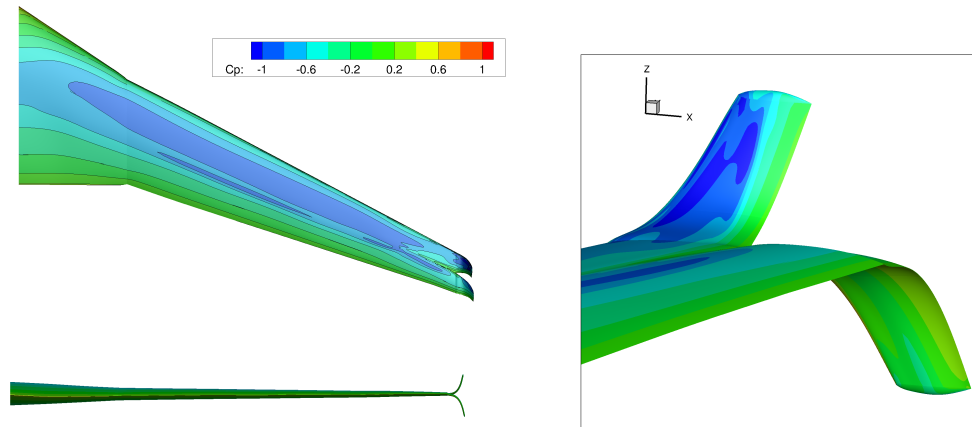
The wingtip fence shows a significant improvement in drag compared to the initial geometry, despite having the greatest wetted area. An interesting feature in this case is that the downward facing tip is tapered less and has greater area than the upward tip. While both wingtips are initially level in the split-tip, the optimizer moves the forward tip upward and the aft tip downward, which agrees with results from Hicken and Zingg.<sup>31</sup> In both of these two cases, the downward wingtip has wash-out and the upward wingtip has wash-in. While the optimized split-tip geometry bears some resemblance to the wingtip fence, it appears to have a higher drag due to the geometry at the junction at the two tips, which presented some difficulty for the solver.



(a) Optimized winglet up



(b) Optimized wingtip fence



(c) Optimized split-tip

Figure 21: Optimized geometries and wingtips for winglet up, wingtip fence and split-tip configurations

## IV. Conclusions

The results of the five optimization problems presented in this paper demonstrate the capabilities of the optimization methodology Jetstream. The CRM wing-only optimization was revisited and results show that the optimizer is still able to make substantial improvements in drag despite increased thickness constraints. Starting from various user-generated initial geometries, different optimization runs indicate that the problem posed for the ADODG benchmark problem 4 is likely not multi-modal. In the trimmed optimization of the CRM wing-body-tail geometry, Jetstream was able to trim the aircraft while reducing the drag by around 2%. The multi-point optimizations of the RAE 2822 airfoil produced much better behaved results than the originally posed single-point problem, and in the case of the second multi-point problem, demonstrated Jetstream's ability to handle low Mach number lift constraints as well as dive conditions that can be challenging for the flow solver.

The last two cases demonstrate the ability of the methodology used by Jetstream to handle successfully optimization problems involving large geometric changes. Starting from a rectangular wing with NACA 0012 sections, the optimizer is able to make substantial changes in both planform and wing section to produce a wing suitable for flow at two different Mach numbers used commonly for commercial air transport. Finally, the study of wing-tip devices on the B737-900 wing geometry illustrates the algorithm's ability to handle non-planar aerodynamic geometries.

## Acknowledgements

The authors gratefully acknowledge the financial assistance from the National Sciences and Engineering Research Council, the Ontario Graduate Scholarship program, and the University of Toronto. Computations were performed on the GPC supercomputer at the SciNet HPC Consortium, part of Compute Canada. Scinet is funded by: the Canada Foundation for Innovation under the auspices of Compute Canada, the Government of Ontario, Ontario Research Fund - Research Excellence, and the University of Toronto.

## References

- <sup>1</sup>Ledoux, S. T., Young, D. P., Fugal, S., Elliot, J., Huffman, W. P., and Melvin, R. G., “An Updated Study for the AIAA Aerodynamic Design Optimization Design Group Test Case-4,” *AIAA Science and Technology Forum and Exposition 2014: 53rd Aerospace Sciences Meeting*, No. AIAA 2015-1717, Kissimmee, Florida, January 2015.
- <sup>2</sup>Chen, S., Lyu, Z., Kenway, G. K. W., and Martins, J. R. R. A., “Aerodynamic Shape Optimization of the Common Research Model Wing-Body-Tail Configuration,” *53rd AIAA Aerospace Sciences Meeting*, No. AIAA 2015-1718, Kissimmee, Florida, January 2015.
- <sup>3</sup>Anderson, G. R., Nemec, M., and Aftosmis, M. J., “Aerodynamic Shape Optimization Benchmarks with Error Control and Automatic Parameterization,” *53rd AIAA Aerospace Sciences Meeting*, No. AIAA 2015-1719, Kissimmee, Florida, January 2015.
- <sup>4</sup>Gariépy, M., Malouin, B., Tribes, C., and Trepanier, J. Y., “Direct Search Airfoil Optimization Using Far-Field Drag Decomposition Results,” *53rd AIAA Aerospace Sciences Meeting*, No. AIAA 2015-1720, Kissimmee, Florida, January 2015.
- <sup>5</sup>Iuliano, E. and Quagliarella, D., “Evolutionary Optimization of Benchmark Aerodynamic Cases using Physics-based Surrogate Models,” *53rd AIAA Aerospace Sciences Meeting*, No. AIAA 2015-1721, Kissimmee, Florida, January 2015.
- <sup>6</sup>Fusi, F., Quaranta, G., Guardone, A., and Congedo, P. M., “Drag minimization of an isolated airfoil in transonic inviscid flow by means of genetic algorithms,” *53rd AIAA Aerospace Sciences Meeting*, No. AIAA 2015-1722, Kissimmee, Florida, January 2015.
- <sup>7</sup>Masters, D. A., Taylor, N. J., Rendall, T. C. S., Allen, C. B., and Poole, D. J., “Review of Aerofoil Parameterisation Methods for Aerodynamic Shape Optimisation,” *53rd AIAA Aerospace Sciences Meeting*, No. AIAA 2015-0761, Kissimmee, Florida, January 2015.
- <sup>8</sup>Meheut, M., Destarac, D., Carrier, G., Anderson, G., Nadarajah, S., Poole, D., Vassberg, J., and Zingg, D. W., “Gradient-Based Single and Multi-point Aerodynamic Optimizations with the elsA Software,” *53rd AIAA Aerospace Sciences Meeting*, No. AIAA 2015-0263, Kissimmee, Florida, January 2015.
- <sup>9</sup>Lee, C., Koo, D., Telidetzki, K., Buckley, H., and Zingg, D. W., “Aerodynamic Shape Optimization of Benchmark Problems using Jetstream,” *AIAA Science and Technology Forum and Exposition 2014: 53rd Aerospace Sciences Meeting*, No. AIAA 2015-0262, Kissimmee, Florida, January 2015.
- <sup>10</sup>Gagnon, H. and Zingg, D., “Two-level free-form and axial deformation for Exploratory Aerodynamic Shape Optimization,” *AIAA Journal*, Vol. 53, No. 7, July 2015, pp. 2015–2026.
- <sup>11</sup>Gagnon, H. and Zingg, D. W., “Euler-Equation-Based Drag Minimization of Unconventional Aircraft Configurations,” submitted to *Journal of Aircraft*, June 2015.
- <sup>12</sup>Gagnon, H. and Zingg, D. W., “Aerodynamic Optimization Trade Study of a Box-Wing Aircraft Configuration,” accepted by *Journal of Aircraft*, August 2015.
- <sup>13</sup>Reist, T. A. and Zingg, D. W., “Aerodynamic Design of Regional-Class Blended Wing-Body Aircraft Through High-Fidelity Aerodynamic Shape Optimization,” submitted to *Journal of Aircraft*, November 2015.
- <sup>14</sup>Hicken, J. E. and Zingg, D. W., “Aerodynamic Optimization with Integrated Geometry Parameterization and Mesh Movement,” *AIAA Journal*, Vol. 48, No. 2, February 2010, pp. 401–413.
- <sup>15</sup>Truong, A. H., Oldfield, C. A., and Zingg, D. W., “Mesh movement for a Discrete-Adjoint Newton-Krylov Algorithm for Aerodynamic Optimization,” *AIAA Journal*, Vol. 46, No. 7, 2008, pp. 1695–1704.
- <sup>16</sup>Hicken, J. E. and Zingg, D. W., “Parallel Newton-Krylov solver for the Euler equations discretized using simultaneous approximation terms,” *AIAA Journal*, Vol. 46, No. 11, November 2008, pp. 2773–2786.
- <sup>17</sup>Osusky, M. and Zingg, D. W., “A Parallel Newton-Krylov-Schur Flow Solver for the Reynolds-averaged Navier-Stokes Equations discretized using summation-by-parts operators,” *AIAA Journal*, Vol. 51, No. 12, December 2013, pp. 2833–2851.
- <sup>18</sup>Jameson, A., Schmidt, W., and Turkel, E., “Numerical solutions of the Euler equations by finite volume methods using Runge-Kutta time-stepping schemes,” *14th Fluid and Plasma Dynamics Conference*, No. AIAA-81-1259, Palo Alto, California, 1981.
- <sup>19</sup>Pulliam, T. H., “Numerical Techniques for Viscous Flow Computation in Turbomachinery Bladings,” Tech. rep., The von Kármán Inst. for Fluid Dynamics, Rhode-Saint-Genèse, Belgium, 1986.
- <sup>20</sup>Swanson, R. C. and Turkel, E., “On central-difference and upwind schemes,” *Journal of Computational Physics*, Vol. 101, No. 2, 1992, pp. 292–306.
- <sup>21</sup>Nocedal, J. and Wright, S., *Numerical Optimization*, Springer series in operations research and financial engineering, Springer, 1999.
- <sup>22</sup>Hicken, J. E. and Zingg, D. W., “A simplified and flexible variant of GCROT for solving nonsymmetric linear systems,” *SIAM Journal on Scientific Computing*, Vol. 32, No. 3, June 2010, pp. 1672–1694.
- <sup>23</sup>Gill, P., Murray, W., and Saunders, M. A., “SNOPT: An SQP Algorithm for Large-Scale Constrained Optimization,” *SIAM Review*, Vol. 47, 2005, pp. 99–131.
- <sup>24</sup>Lyu, Z., Kenway, G. K. W., and Martins, J. R. R. A., “Aerodynamic Shape Optimization Investigations of the Common Research Model Wing Benchmark,” *AIAA Science and Technology Forum and Exposition*, No. AIAA-2014-0567, National Harbor, Maryland, January 2014.
- <sup>25</sup>Osusky, L., Buckley, H. P., Reist, T. A., and Zingg, D. W., “Drag Minimization based on the Navier-Stokes equations using a Newton-Krylov approach,” *AIAA Journal*, Vol. 53, No. 6, June 2015, pp. 1555–1577.
- <sup>26</sup>Ledoux, S. T., Vassberg, J. C., Young, D. P., Fugal, S., Kamenetskiy, D., Huffman, W. P., Melvin, R. G., and Smith, M. F., “Study Based on the AIAA Aerodynamic Design Optimization Discussion Group Test Cases,” *AIAA Journal*, Vol. 53, No. 7, July 2015, pp. 1910–1935.
- <sup>27</sup>Nemec, M., Zingg, D. W., and Pulliam, T. H., “Multipoint and Multi-Objective Aerodynamic Shape Optimization,” *AIAA Journal*, Vol. 42, No. 6, June 2004, pp. 1057–1065.

<sup>28</sup>Buckley, H. P. and Zingg, D. W., “An Approach to Aerodynamic Design through Numerical Optimization,” *AIAA Journal*, Vol. 51, No. 8, August 2013.

<sup>29</sup>Buckley, H. P., Zhou, B. Y., and Zingg, D. W., “Airfoil Optimization using Practical Aerodynamic Design Requirements,” *Journal of Aircraft*, Vol. 47, No. 5, October 2010.

<sup>30</sup>Wrenn, G. A., “An Indirect Method for Numerical Optimization Using the Kreisselmeier-Steinhauser Function,” Tech. Rep. CR-4220, NASA, 1989.

<sup>31</sup>Hicken, J. E. and Zingg, D. W., “Induced-Drag Minimization of Nonplanar Geometries Based on the Euler Equations,” *AIAA Journal*, Vol. 48, No. 11, November 2010, pp. 2564–2575.

<sup>32</sup>Khosravi, S. and Zingg, D. W., “A Numerical Optimization Study on Winglets,” *15th AIAA/ISSMO Multidisciplinary Analysis and Optimization Conference*, No. AIAA 2014-2173, Atlanta, Georgia, U.S.A., June 2014.